Universiteit Utrecht
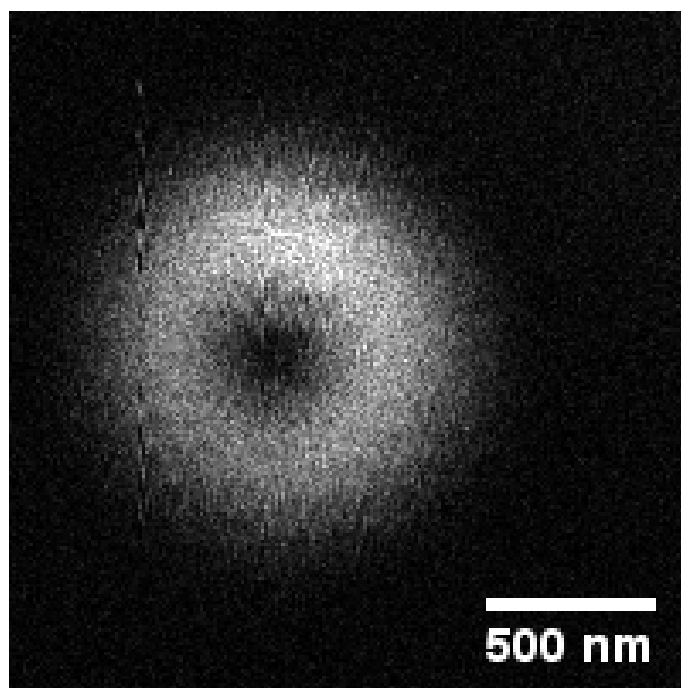
Optimization of a Doughnut Shaped Depletion Beam Using a Spatial Light Modulator

Author:
Stefan Verheul
Study: Physics & Astronomy

Supervisor:
Dr. G.A. Blab
Utrecht University

15 June 2016

Abstract

In conventional (fluorescent) microscopy, the wave-like properties of light set a limit on the maximum achievable image resolution . This limit is known as the Abbe diffraction limit. The last few decades, techniques have been developed to overcome this limit and thereby improve the resolution.

One such a super-resolution technique is called Stimulated Emission Depletion microscopy (STED). The key feature of STED is the use of an excitation beam in combination with an overlapping ring shaped depletion beam with a central minimum. The excitation spot is used to push the fluorophores in an excited state. The depletion beam will in turn deplete (switch off) a part of the outer region of the diffraction limited excitation spot. Therefore, focus spot is reduced to a size which is smaller than stated by the diffraction limit. This way, the resolution can be improved beyond the diffraction limit.

In this bachelor research project, a simplified STED setup is used to optimize the rotational symmetry of the depletion beam. An essential part used in doing so is the Spatial Light Modulator (SLM). The SLM can be used to shape foci in an almost arbitrary way by locally changing the phase of light. The depletion beam was generated by applying a vortex phase pattern on the SLM. Furthermore, it was possible to characterize and correct for aberrations due to imperfections of the optical system. Also, the alignment of the setup and the polarization direction of the beam were systematically adjusted in order to obtain a rotational symmetric doughnut. Finally, the shape and size of the imaged fluorescent beads were analyzed taken into account the polarization, misalignment and aberrations of the optical system.

Contents

Chapter 1

Introduction

Ever since the invention of the microscope around 300 years ago, people have tried to reveal the world far below the millimetre scale, impossible to observe with the naked eye. Anthony van Leeuwenhoek already observed bacteria back in 1676 Win. However, as microscopes became more advanced, the resolution increased close to the resolution limit which depends on the light's wavelength. Increasing the resolution by lowering the wavelength could result in the destruction of the sample under investigation, as the corresponding photon energies will be higher.

In order to circumvent the so called diffraction limit, numerous super-resolution microscopy techniques were developed the last few decades. In this thesis I have focussed on one such a technique which is named Stimulated Emission Depletion (STED) microscopy. A key role in this technique is played by a doughnut shaped focus, which crucially determines the maximum obtainable resolution. I tried to optimize the quality of this doughnut shape via the use of a Spatial Light Modulator (SLM). Via the use of a Spatial Light Modulator (SLM) I tried to optimize the quality of this doughnut shape and quantify the wavefront distortions caused by the optical components in the setup.

Chapter 2

Theory

2.1 Theory

In this section the concept of fluorescence microscopy, it's resolution limit and a technique to circumvent this limit (STED Microscopy) are discussed. Afterwards, theoretical intensity profiles of an ideal focus spot and an doughnut shaped focus spot are derived. Finally, it will be discussed how such a doughnut shape can be realized in practice and how deviations from ideal behaviour can be described.

2.1.1 Fluorescence Microscopy

In fluorescence microscopy, the observed light originates not just from the reflection of the illumination light on the sample. The (in)organic molecules themselves spontaneously emit photons after illumination by a light source.

A crucial part in this microscopy technique, the phenomenon of spontaneous emission, works as follows: An electron of the fluorescent particle is excited to a vibrational energy state S_1^{vib} by absorbing a photon. This photon corresponds to the energy difference of the electron's ground state and the vibrational energy state. After excitation, the state S_1^{vib} relaxes to the lowest energy level of S_1. Now, the electron will fall back to the ground state via either spontaneous emission of a photon or non-radiative decay.
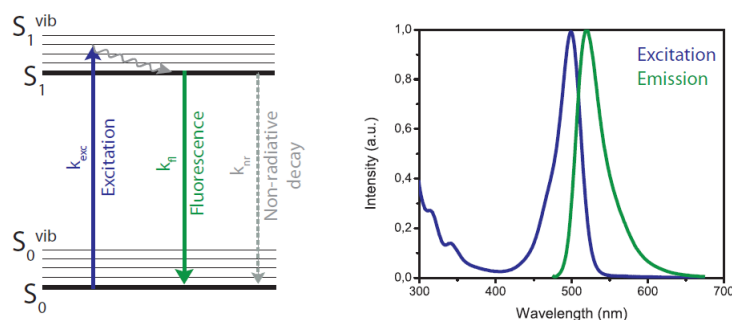

Figure 2.1 – Jablonski diagram showing the process of spontaneous emission together with a graph of an emission and excitation spectrum. The image merely illustrates the process, the wavelengths do not correspond to the one used in the experiments. Picture taken from Dijkstra [2012].

Due to the energy loss in the relaxation of S_1^{vib} to S_1, the photon energy of the spontaneous emission is lower in comparison with the excitation energy. This leads to a red shifted emission profile as shown in 2.1.

If the light from spontaneous emission is separated from the excitation light using an emission filter, the position of the fluorescent particles can be determined.
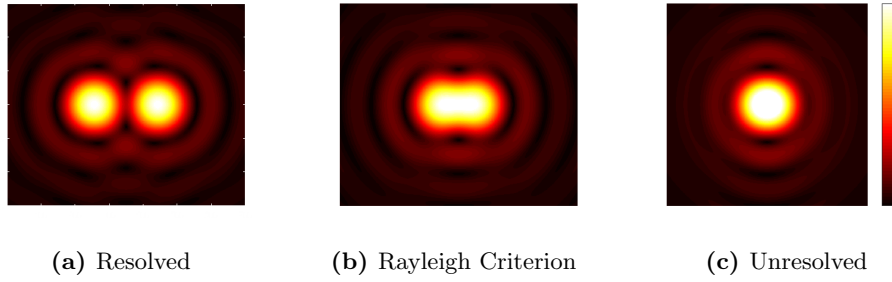
(a) Resolved   **(b)** Rayleigh Criterion   **(c)** Unresolved

Figure 2.2 – PSF of two particles at spatial separation R of (a) $R = 2d$, clearly resolved; (b) the Rayleigh Criterion, $R = d$, barely resolved; (c) $R < d$, unresolved.

2.1.2   Diffraction Limit

Due to the wave-like nature of light, the maximum obtainable image resolution of a microscope is limited by the diffraction limit. This limit was first stated by Ernst Abbe in 1873 Abbe [1874]. It implies that focused light will converge into a spot of radius d which depends on the used wavelength λ, the refractive index of the medium n and the angle of the focused light θ. In section 2.1.5 it is shown that for a plane wave incident on a circular aperture, the diffraction limit takes on the form:

$$d = 1.22\frac{\lambda}{2n\sin\theta} = 1.22\frac{\lambda}{2\text{NA}} \tag{2.1.1}$$

In which the denominator is rewritten in terms of the numerical aperture $\text{NA} = n\sin\theta$, often used to describe the properties of a microscope.

The spot size d is intimately related to the resolution. To explain this, another frequently encountered concept in microscopy is needed. The Point Spread Function (PSF) describes the diffraction limited intensity distribution one would get when imaging a single point object. In an ideal optical system this PSF is an Airy Disk pattern (further explained in section 2.1.5) with radius d.

In a more mathematical sense the imaging of an object is described by a convolution of the object with the PSF. This means that if one tries to image two point objects, they will show up as two bright spots with a radius of at least d. Now, if two objects are separated by a distance smaller than $2d$, the image will show two overlapping PSFs. Though, up to a separation of distance d, two particles can still be resolved. At even smaller distances the particles are unresolvable since the convolutions will merge as shown in figure 2.2c. The spatial resolution of an optical system thus depends on the focus spot size, equal to the minimum distance at which two particles are resolvable.

This has implications for fluorescence microscopy as well. If a sample of point particles is illuminated by a finite size excitation spot, all the particles within this spot will exhibit spontaneous emission. Those close enough to eachother would be unresolvable due to the diffraction limit, thereby losing detailed information about the fluorophore positions. In the experimental setup an objective with a NA of 1.2 was used in combination with a 642 nm laser. The maximum obtainable resolution is thus 330 nm.

2.1.3   Stimulated Emission Depletion Microscopy

In order to overcome the diffraction limit and obtain images of even greater detail, a range of so called super-resolution techniques have been developed. One such a super-resolution technique is Stimulated Emission Depletion microscopy (STED) and was first proposed by Stefan W. Hell in 1994 Hell and Wichmann [1994].

The key feature of STED is a doughnut shaped depletion beam in combination with an excitation spot. The depletion beam is used to switch off the fluorophores on the outer ring of the area illuminated by the excitation beam. This process is shown in the Jablonski diagram in 2.3. An electron in state S_1 is de-excited to a state S_0^{vib} by the depletion beam after it will relax to state S_0. This process of stimulated emission

is represented by the yellow arrow in the Jablonski diagram. An important remark is that the dark centre of the doughnut spot will not cause stimulated emission. Therefore, spontaneous emission is confined to the area excluded by this depletion beam. Moreover, the different wavelengths at which spontaneous and stimulated emission are most efficient can be exploited to only detect the fluorescence signal using appropiate filters.
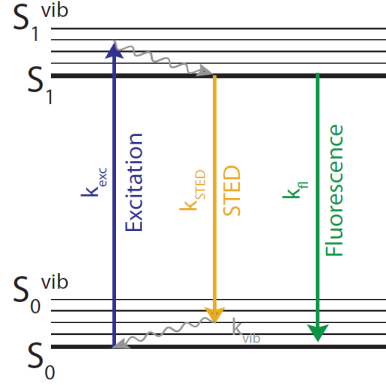

Figure 2.3 – Jablonski diagram showing the process of STED. The colors are no representation of the corresponding wavelengths of wavenumbers k_{exc}, k_{STED} and k_{fl}. Picture from Dijkstra [2012]

Depletion Beam Quality

The size, quality and intensity of the depletion beam crucially determine the size of the remaining fluorescence spot and thus the resolution.

The center minimum of the depletion beam has to be as close to zero as possible. Otherwise, the remaining fluorescence signal will be reduced without enhancing the resolution.

The radius of the center minimum determines the area from which fluorescence signal can be collected. Therefore, a smaller radius makes a higher obtainable resolution.

The relative intensities of the depletion and excitation beams determine the size of the remaining spot. Sufficient de-excitation is needed to achieve a high resolution.

Also, the depletion beam has to be rotational symmetric. Otherwise, the fluorescence signal may no longer solely originate from the center spot and the center intensity may no longer be close to zero.

The focus of this bachelor research project lies within the characterization and optimization of the depletion beam's shape. The center intensity minimum and the ring shape are analyzed and optimized as to acquire a rotational symmetric depletion pattern.

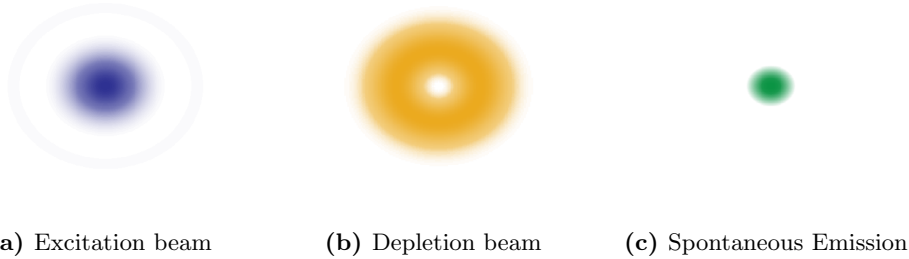(a) Excitation beam   (b) Depletion beam   (c) Spontaneous Emission

Figure 2.4 – Images illustrating the STED process: (a) The excitation beam, (b) the depletion beam forcing the fluorophores in the outer region of the excitation beam to de-excite, (c) the area in which spontaneous emission can still occur is decreased.

2.1.4 Diffraction From a Circular Aperture

Before investigating the intensity distribution of a beam diffracted by a circular aperture, a short theoretical background of the aperture diffraction based on Born and Wolf [2000] and de Boer [2015] is given in this section of which the result is stated by equation 2.1.8. After switching polar coordinates, the intensity distributions of an ordinary focus spot and a doughnut shaped focus are derived.

Kirchhoff derived an approximate scalar solution to the homogeneous wave equation for the case of a wave diffracted by an arbitrarily shaped aperture. The solution at an arbitrary point P is given in terms of values of the wave equation solution and the first derivatives on a surface enclosing P. In the case of a monochromatic wave source this solution is:

$$U(P) = -\frac{iU_0}{2\lambda} \iint_S \frac{e^{ik(r+s)}}{rs} [\cos(n,r) - \cos(n,s)] dS \tag{2.1.2}$$

In which S is the area of integration corresponding to Σ, U_0 is the initial disturbance at point P_0, r is the distance from point P_0 to aperture point P_1, s is the distance between P_1 and image point P and (n,r) and (n,s) are the angles between the aperture plane normal and unit vectors $\hat{r}$ and $\hat{s}$ respectively (see figure 2.5

Huygens-Fresnel equation

If it is assumed that a plane wave is incident on a circular aperture, the Kirchhoff integral reduces to the more familiar Huygens-Fresnel equation:

$$U(P) = -\frac{i}{2\lambda} \frac{U_0 e^{ikr}}{r} \oint_{A_1} \frac{e^{iks}}{s} (1 + \cos(r,s)) dS \tag{2.1.3}$$

The advantage of the Kirchhoff integral is that the factor i/λ and the cosine term are mathematically derived and follow as a consequence of the wave-nature of light. Fresnel had to assign these terms as corrections in order to obtain agreement with his measurements.

Fraunhofer Diffraction

Fraunhofer diffraction is valid when the diffracted wave is observed in the far field or when a lens is used to focus the light.

To obtain a solution at point P in the image plane, a few approximations are made. The first one simplifies the factor $1 + \cos(r,s)$. If the source and image points P_0 and P are situated at a distance larger than the aperture size, the angles made with the aperture will not vary too much. Under the assumption of a plane incident wave, the cosine factor is replaced with $2\cos\theta$ in which θ is the angle between P_1, P and the aperture normal. Before applying a second approximation we switch to a Cartesian reference system as shown in figure 2.5. The aperture is situated in the (ξ,η)- plane around the origin and point P in the (x,y)-plane, a normal distance z separated from the aperture screen. From geometric considerations it follows that the distance between $P_1(\xi,\eta)$ and $P(x,y)$ equals:

$$s = z\sqrt{1 + \left(\frac{\xi - x}{z}\right)^2 + \left(\frac{\eta - y}{z}\right)^2} \tag{2.1.4}$$

Reconsidering the first assumption, it follows that $z \gg \xi - x$ and $z \gg \eta - y$. A first order expansion of the expression for s can therefore be made:

$$s \approx z\left[1 + \frac{1}{2}\left(\frac{\xi - x}{z}\right)^2 + \frac{1}{2}\left(\frac{\eta - y}{z}\right)^2\right] \tag{2.1.5}$$

The full expression of the integral becomes:

$$U(x,y) = \frac{ie^{ikz}}{\lambda z} e^{\frac{ik}{2z}(x^2+y^2)} \int\int_\Sigma U(\xi,\eta) e^{\frac{ik}{2z}(\xi^2+\eta^2)} e^{-\frac{ik}{\lambda z}(\xi x+\eta y))} d\xi d\eta \tag{2.1.6}$$
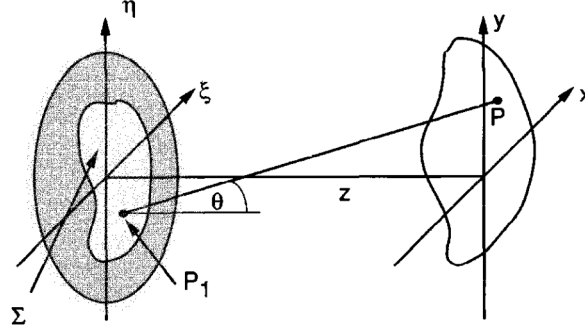
Figure 2.5 – Geometry of the cartesian reference system [REF]

This integral can be greatly simplified since the far field approximation

$$z \gg \frac{k(\xi^2 + \eta^2)_{max}}{2} \tag{2.1.7}$$

holds. As a consequence, the factor $exp[\frac{ik}{2z}(\xi^2 + \eta^2)]$ is approximately unity over the aperture area Σ. Now, 2.1.6 takes the form:

$$U(x, y) \propto \iint\limits_{\Sigma} U(\xi, \eta) e^{-\frac{ik}{\lambda z}(\xi x + \eta y)} d\xi d\eta \tag{2.1.8}$$

With constant C containing all the prefactors, $U(\xi, \eta)$ the complex amplitude of the disturbance in the aperture and (x,y) .

2.1.5 Airy Disk

In this section the Fraunhofer diffraction pattern resulting from a monochromatic, uniform plane wave incident on a circular aperture is calculated based on the derivations given by Born and Wolf [2000] and de Boer [2015]. The resulting intensity distribution in the plane of focus goes by the name of an 'Airy Disk' pattern. The starting point for this derivation is equation 2.1.8.

The aperture's rotational symmetry suggests using polar coordinates. Let (ρ, ϕ) be the coordinates of the aperture and (q, Φ) the coordinates of the image plane.

$$\rho \cos \phi = \xi \qquad \rho \sin \phi = \eta \tag{2.1.9}$$

$$q \cos \Phi = x \qquad q \sin \Phi = y \tag{2.1.10}$$

Rewriting the differential area element gives:

$$dS = \rho d\rho d\phi \tag{2.1.11}$$

The radius of the circular aperture is taken to be a. Equation 2.1.8 expressed in the cylindrical coordinates as specified above now becomes:

$$U(q, \Phi) \propto \int_{\phi=0}^{2\pi} \int_{\rho=0}^{a} U(\rho, \phi) e^{-\frac{ik\rho q}{z} \cos(\phi - \Phi)} \rho d\rho d\phi \tag{2.1.12}$$

Since the incident wave is assumed to be a plane, the intensity at the aperture is independent of ρ and ϕ. Therefore, $U(\rho, \phi) = 1.0$. In addition assume that the aperture's symmetry causes the far field to possess rotational symmetry as well. The solution of the

integral must then be independent of Φ. Therefore, $\Phi = 0$ is assigned to further simplify the integral:

$$U(q) \propto \int_{\phi=0}^{2\pi} \int_{\rho=0}^{a} e^{-\frac{ik\rho q}{z} \cos(\phi)} \rho d\rho d\phi \tag{2.1.13}$$

Now, the ϕ dependent part is similar to a zeroth order Bessel function which is defined as:

$$J_0(u) = \frac{1}{2\pi} \int_0^{2\pi} e^{iu \cos \nu} d\nu \tag{2.1.14}$$

Setting $u = k\rho q/z$ and $\nu = \phi$. and using the identity:

$$\int_0^u u' J_0(u') du' = u J_1(u), \tag{2.1.15}$$

The integral (eq. 2.1.13) can now be rewritten in terms of a first order Bessel function:

$$U(q) \propto \frac{2\pi a^2}{z} \frac{J_1(kaq/z)}{kaq/z} \tag{2.1.16}$$

Now, a lens with focal distance f is placed in the aperture. The intensity distribution is therefore situated at the focus point of the lens while the validity of the far field approximation is maintained. Therefore, the intensity distribution $I(q)$ at the focus f is given by:

$$I(q) = |U(q)|^2 = I_0 \left[2\frac{J_1(kaq/f)}{kaq/f} \right]^2 \tag{2.1.17}$$

In which I_0, the center intensity, contains all constant prefactors.

The calculated intensity distribution is called an Airy Disc. It has a central maximum surrounded by rings of decreasing intensity as shown in FIGURE X. Substitution of kaq/f with more usually encountered experimental constants numerical aperture NA and wavelength λ leads to the final expression of the Airy Disk:

$$I(q) = I_0 \left[2\frac{J_1\left(\frac{2\pi q \text{NA}}{\lambda}\right)}{\left(\frac{2\pi q \text{NA}}{\lambda}\right)} \right]^2 \tag{2.1.18}$$

It is readily seen that the focal spot size is critically dependent on the NA of the objective and the wavelength of the laser light.

The first minimum of the Airy pattern, i.e. the radius of the first dark ring occurs when $J_1(2\pi \text{NA}q/\lambda) = 0$. This is the case when $2\pi \text{NA}q/\lambda = 1.220\pi$. Solving for q gives the earlier encountered Abbe limit for diffraction from a circular aperture, stated in equation 2.1.1.

2.1.6 Doughnut Profile

In order to create a doughnut pattern instead of an Airy Disk, the incident uniform beam has to be shaped such that the light will show a minimum intensity in the center of the focus. This can be done by modulating the phase distribution in such a way as to cause the light in beam's center to interfere destructively. A phase distribution which meets this requirements is called a vortex phase pattern and, as mentioned in the introduction, a Spatial Light Modulator (SLM) is used for this purpose. This section is focussed on the derivation of a dougnut shaped intensity profile as given by Neupane, Chen, Sun, Chiu, and Wang [2013] and de Boer [2015].

Optical Vortex

When light is twisted like a screw around the direction of propagation, one speaks of an optical vortex. An optical vortex is characterized by it's vorticity, the total phase difference after travelling one wavelength. Vorticity is defined as $V = 2\pi|n|$ with n the topological charge, an integer number. An example of a vortex with a topological charge $n = 1$ is shown in 2.6.
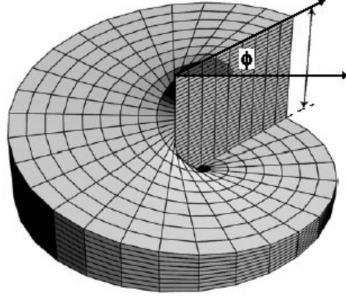
Figure 2.6 – Vortex with topological charge $n = 1$. Picture from Leach et al. [2005].

If an optical vortex falls on a screen perpendicular to the axis of propagation, the wavefront will appear as a ring shaped pattern with a central intensity minimum will appear. This concept will now be used to derive a doughnut profile after a plane wave is diffracted by a circular aperture.

Doughnut Profile from Circular Aperture Diffraction

Starting with equation 2.1.12, the incident bundle $U(\rho, \Phi)$ will now have a phase which changes linearly with the angle Φ. Assuming a vorticity of 2π, the expression for $U(\rho, \Phi)$ can be rewritten, instead of unity it becomes:

$$U(\Phi) = e^{i\Phi} \tag{2.1.19}$$

Equation 2.1.12 can now be rewritten:

$$U(q, \phi) \propto \int_0^a \int_0^{2\pi} e^{i(\Phi + \frac{k\rho q}{z})cos(\phi)} d\phi \rho d\rho \tag{2.1.20}$$

Somewhat similar as in the previous section, a Bessel function can be recognized:

$$J_1(u) = \frac{1}{i2\pi} \int_0^{2\pi} e^{i(\nu + u\,cos(\nu))} d\nu \tag{2.1.21}$$

This integral can in turn be approximated using a Struve function $H_n(u)$.

$$\int_0^u J_1(u')u' du' = \frac{\pi}{2} u[J_1(u)H_0(u) - J_0(u)H_1(u)] \tag{2.1.22}$$
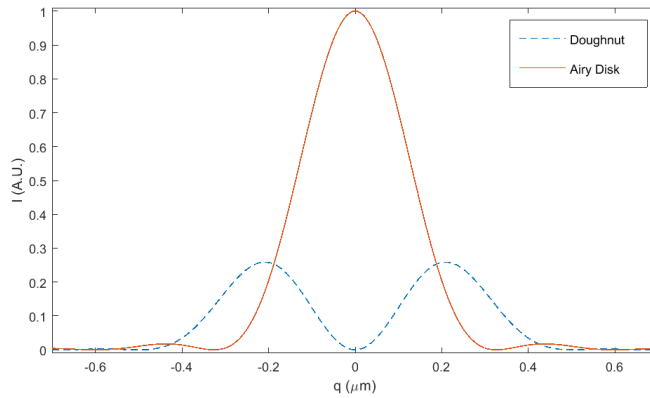

Figure 2.7 – Calculated intensity distributions for the Airy Disk (solid line) and the 2π-doughnut (dashed line) using a wavelength of 642 nm and a NA of 1.2.

Now, the intensity distribution is rewritten in the experimentally useful terms NA and λ:

$$I(q) = I_0 \left[\pi \frac{J_1\left(\frac{2\pi q \mathrm{NA}}{\lambda}\right)H_0\left(\frac{2\pi q \mathrm{NA}}{\lambda}\right) - J_0\left(\frac{2\pi q \mathrm{NA}}{\lambda}\right)H_1\left(\frac{2\pi q \mathrm{NA}}{\lambda}\right)}{\frac{2\pi q \mathrm{NA}}{\lambda}} \right]^2 \tag{2.1.23}$$

This intensity distribution is shown together with the Airy Disk in figure X. As expected, the doughnut profile shows a zero intensity in the center. In comparison with the Airy Disk, the doughnut distribution is spread out over a greater area and since a phase modulation does not affect the total intensity, the maxima are lower. Doughnut patterns of topological charge $n > 1$ will not only increase the focus size which is in conflict with the goal of increasing the resolution. Therefore, only the doughnut profile resulting from topological charge $n = 1$ will be used.

2.1.7 Spatial Light Modulator and Zernike Polynomials

There are several ways of applying a vortex phase pattern to a beam of light. Frequently used optical components for this purpose are a vortex phase plate and a Spatial Light Modulator (SLM). For the experiments done a SLM was used to create the depletion pattern. An major advantage of a SLM over a phase plate is that it can shape foci in an almost arbitrary way. Since an experimental setup is not an ideal optical system, aberrations and misalignments will cause the depletion pattern to be deviated form its ideal shape. The SLM can be used to correct for these deviations as well.

Kinoforms

The SLM has a liquid crystal display which can modulate the phase of light. Each pixel can be controlled by applying a voltage to it, thereby modifying the liquid crystals in such a way as to cause the desired phase pattern. These phase patterns are called Kinoforms and can be applied to SLM. The SLM will in turn convert the desired phase delay to pixel values specific for the used wavelength.

The central kinoform used in obtaining a doughnut profile is shown 2.6, corresponding to a vorticity of 2π. The gray levels represent a phase delay in which black and white correspond to a phase delay of 0 and 2π, respectively. Obviously, a phase shift of (a multiple of) 2π is the same as a phase shift of 0. As already mentioned, the SLM can
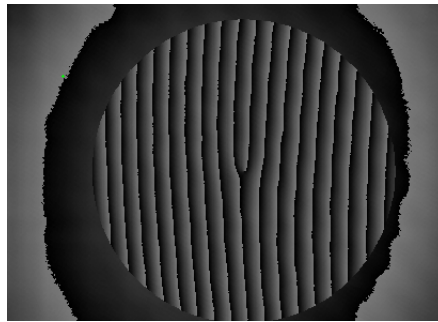

Figure 2.8 – Example of a kinoform as applied on the SLM in which a wavelength dependent calibration pattern, tilt, astigmatism and a vortex phase mask are superimposed.

be used to correct for misalignments and aberrations caused by the optical components in the setup. The additional correction kinoforms can be superimposed on the vortex kinoform as shown in 2.8.

Zernike Polynomials

A common way to characterize wavefronts in optics is via the use of Zernike Polynomials. Zernike Polynomials are a complete set of orthogonal polynomials on the unit disk. Although there are many orthogonal sets, the polynomials first described by Frits Zernike

**Table 2.1** – Mathematical form of the Zernike Polynomials as applied on the SLM

Form of the Polynomial	(n,m)	Name
$\rho \cos \phi$	(1, 1)	Tilt-X
$\rho \sin \phi$	(1,-1)	Tilt-Y
$\rho^2 \cos 2\phi$	(2, 2)	Astigmatism-Y
$\rho^2 \sin 2\phi$	(2,-2)	Astigmatism-X
$(3\rho^2 - 2\rho)\rho \cos \phi$	(3, 1)	Coma-X
$(3\rho^2 - 2\rho)\rho \sin \phi$	(3,-1)	Coma-Y

are of great practical use since each polynomial corrresponds to an often encountered wavefront aberration Wyant and Creath [1992]. In general, each polynomial consists of a nth order radial polynomial $R_n^m(\rho)$ and an angular, ϕ-dependent part. The sign of the integer m indicates whether a cos or sin function is used while it's value indicates the frequency of peaks and valleys encountered going round the unit disk zer [a].

$$Z_n^m(\rho, \phi) = R_n^m(\rho) \cos(m\phi) \tag{2.1.24}$$

$$Z_n^{-m}(\rho, \phi) = R_n^m(\rho) \sin(m\phi) \tag{2.1.25}$$

An in-depth description of the Zernike Polynomials can be found in Born and Wolf [2000]. The relevant polynomials used in the experiments as described in chapter 3 are tip, tilt, astigmatism and coma. These aberrations correspond to the polynomials Z_1^1, Z_1^{-1} for tip (Tilt-X) and tilt (Tilt-Y), Z_2^2, Z_2^{-2} for vertical astigmatism (Astigmatism-Y) and oblique astigmatism (Astigmatism-X) and Z_3^1, Z_3^{-1} for vertical coma (Coma-X) and horizontal coma (Coma-Y) as listed in table 2.1. A tip or tilt will cause the focus to shift in the lateral x,y-direction, respectively. When two perpendicular planes of light incident on a lens with a certain amount of astigmatism, the planes are focussed at different distances from the lens. This type of aberration is caused by rotational asymmetry of optical components. When coma aberration is present, off-axis points incident on a lens are imaged as a spread out Airy Disk.
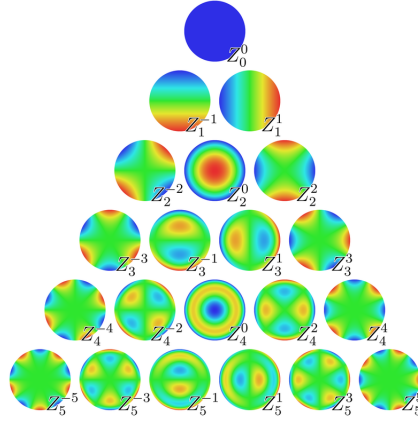
Figure 2.9 – Images of the first 21 Zernike Polynomials zer [b].

With the use of these polynomials, deviations of the wavefront from ideal behaviour will be characterized.

Chapter 3

Experiments and Setup

In this chapter the used setup will be described along with a general description of the conducted experiments. An important part of the setup is the SLM. This will be discussed in a separate section 3.1.1.

3.1 Instrumentation

The simplified STED-setup as used in the experiments is shown in 3.1. It was already build as a part of a previous bachelor research project by B. Brouwer. All the components the emitted laser light meets in its travel from emission by the laser to the detection of the signal will be described.
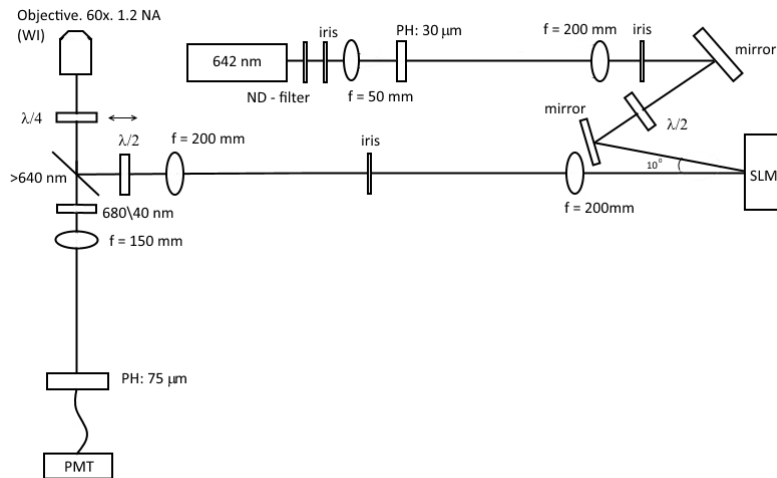

Figure 3.1 – Schematic representation of the used setup. Explanation of the used abbreviations: Neutral Density filter (ND), Pinhole (PH), Spatial Light Modulator (SLM), Photo Multiplier Tube (PMT). Picture from B. Brouwer.

An Omnicron LuxX R laser emitting 642 nm laser light was used as a source. In the configuration used it emitted light of vertical polarization with respect to the table. The beam's diameter was shrunk to 7.2 ± 0.2 mm by an iris to meet the spatial dimensions of the SLM display. The beam passes through a beam expander made of two lenses with focal distances of 50 and 200 mm respectively, and a 30 μm pinhole in between to clean up the beam. Via two mirrors and a $\lambda/2$ wave plate (ThorLabs AHWP05M-600), the beam is converted to horizontally light and reflected to fall under an angle of 5 deg with the SLM (Hamamatsu LCOS-SLM 620-1100nm). The $\lambda/2$ plate ensures the horizontal

polarization of the beam, this is required for optimal modulation of the SLM. The iris in the middle of the two lenses is used to block the reflected, zeroth order light and thereby keeping only the modulated part of the beam. A more detailed discussion concerning the SLM is given in 3.1.1. After the second lens a $\lambda/2$ wave plate is placed to change the polarization to vertical again. This is needed since the dichroic mirror favors vertical polarized light. Before arriving at the back aperture of the objective, a $\lambda/4$ wave plate (ThorLabs AQWP05M-600)is placed to convert the polarization of the beam from linear to circular. The used objective was a Nikon 60x 1.2 NA Water Immersion objective with a 1.0 cm back aperture. The objective focusses the light on a sample of red beads 0.2 µm. Via the use of a piezo stage, the sample could be moved in three dimensions over the fixed objective. The fluorescence of the red beads was collected by the objective and send back through the $\lambda/4$ plate and the dichroic mirror. Then, a 660-700 nm bandpassfilter blocked the remaining parts of the depletion beam. The fluorescence signal (transmitted by the bandpassfilter) was focused by a 150 mm lens into a 75 µm pinhole with a fiber just behind it. The fiber was connected to a Photo Multiplier Tube (PMT) which converted the signal to an electric one. Finally, the electric signal was read out by a computer. And displayed via a custom made LabVIEW program.

3.1.1   The Spatial Light Modulator

For the experiments done, a Hamamatsu LCOS-SLM 620-1100nm was used. The Liquid Crystal Display (LCD) of the SLM has an area of 10 x 7.5 mm and consists out of 792 x 600 pixels. Using a wavelength of 642nm, the SLM can modulate the phase delay of light from 0 to 2π in 127 values. Futhermore, the polarization direction of the incident light has to be aligned with the direction in which the liquid crystal molecules are orientated. Therefore, the polarization of the incident light is horizontal. After the phase modulation, the beam will continue its path as if it is merely reflected by the LCD. However, the SLM will not modulate all the incident light. Part of it is only reflected and will propagate along the same path as the modulated beam. Since only the doughnut shaped beam will be used in the experiments, the reflected (zeroth order) beam and modulated (first order) beam had to be separated. From geometric considerations it can be shown that the relation between the applied tilt n and the spatial separation of the beams is given by:

$$\delta x = 2n\frac{f\lambda}{d} \tag{3.1.1}$$

In which the applied tilt, n, represents the number of 2π phase shift cycles applied over the kinoform. This linear relation of δx and n is shown in figure 3.2. A phase mask
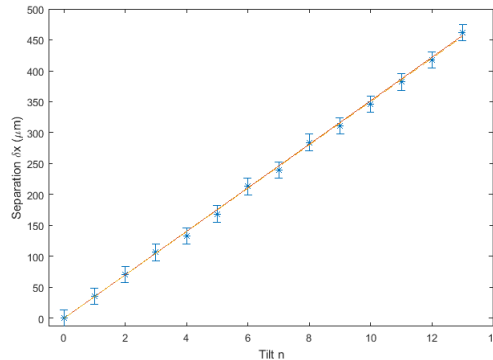

Figure 3.2 – Measured and calculated relation of applied tilt n and beam separation δx at the focus point of the first 200 mm lens, using wavelength $\lambda = 642$ nm and beam diameter $d = 7.2(2)$ mm

corresponding to a tilt of $n = 12$, that is, 12 cycles of 2π phase shift, was applied on the SLM to separate the beams by 0.42(2) mm.

3.2   Description of the Experiments

The focus of the experiments lies in obtaining a rotational symmetric doughnut and analysing the aberrations of the system. The SLM is used to correct for the aberrations. I tried to quantifiy the phase modulations needed to minimize the deviations from the symmetric doughnut pattern. Furthermore, the effect of different polarizations on the shape of the beam were investigated. Simulations Yang, Zhang, Xiao, Gao, Chang, Wei, and Jiang [2016] suggest that the polarization of the beam influences on the beam's shape. Apart from the measurements on polarization itself, circular polarization was used in all experiments.

The experiments involving the optimization of the doughnut shape were conducted in the following order. First, the spatial separation of the reflected and modulated beams as a function of the tilt was measured. The reflected beam was then blocked by an iris. Afterwards, the SLM was used to vary the amount of astigmatism-X of which the results were captured with a camera. After determining the SLM settings for which the doughnut shape was optimized, the corresponding value for the SLM parameter was saved and the amount of astigmatism-Y was varied. In these measurements a mirror instead of a sample will be placed on the objective. Since there will probably be some sample induced aberrations present, this procedure will be repeated with scans of a single bead. If there are no other aberrations in the optical system present and the setup is aligned, I should have obtained a rotational symmetric doughnut. If not, I have to search for possible misalignments or additional aberrations like coma. By making radial and angular intensity profiles of the doughnuts, the SLM settings and aberrations involved will be analysed. By a combination of mechanical alignment, kinoform alignment, phase modulations by the SLM and angular and radial profiles I will characterize and optimize the doughnut shape.

3.2.1   Experimental Details

In this section the experimental details involved in obtaining the results are discussed. During measurements the laser was operated at 1.0mW with a Neutral Density filter of 2.0. A first point of concern was the beam diameter after the beam expander. It did not match the dimensions of the SLM display. The effective area of the SLM display is 10x7.5 mm. The maximum diameter of a beam which can be modulated by the SLM is thus 7.5 mm. However, the beam expander enlarged the beam diameter to around 10 mm. Fortunately, the iris after the beam expander was already set as to reduce the diameter to 7.2(2) mm.

Measurement settings

During the measurements a Tilt-X of 12 was applied on the SLM as to separate and block the zeroth from the first order beam. In order to quickly observe the beam modulations produced by the SLM, a 1600x1200 pixel camera (Nikon DS-2MBWc) was used in place of the last pinhole (the fiber was removed for this purpose). The first astigmatism corrections and kinoform alignment were both observed using this camera, imaging the reflected beam by a mirror on the objective instead of scans of beads. The actual sample scans were conducted using a pixel dwell time of 1 ms and a pixel lag of 3.5 ms. The images consisted out of 200x200 pixels and an area of 2x2 µm, leading to a pixel to pixel distance of 10 nm. The images involving coma corrections were scanned using the same settings and area except 100x100 pixels were used.

Polarization

The SLM modulates only horizontally polarized light. In order to filter out any vertical (and unmodulated) polarized light, a linear polarizer was set behind the HWP near the dichroic mirror. The dichroic mirror favours vertically polarized light. Therefore, the HWP was used to switch the polarization back to vertical. Ideally, the HWP should therefore be placed at 315 deg or 45 deg. However, the actual retardances of the half-
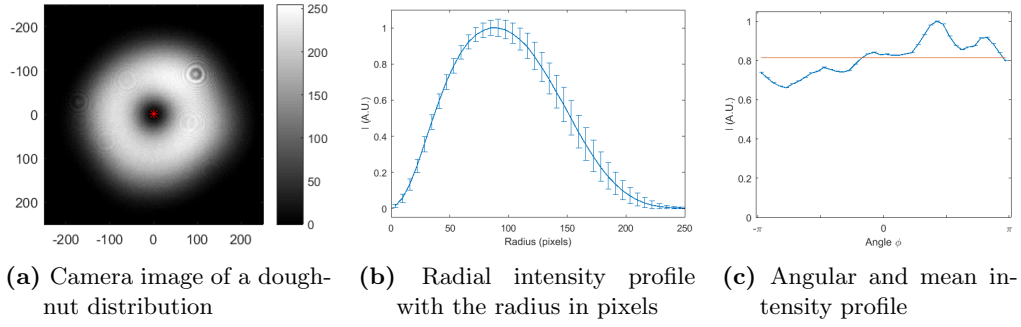
(a) Camera image of a dough-nut distribution

(b) Radial intensity profile with the radius in pixels

(c) Angular and mean intensity profile

Figure 3.3 – Figures illustrating the doughnut pattern analysis written in MATLAB. Aberrations as applied on the SLM: Astigmatism X = 0.1 and Astigmatism Y = 0.3. (A) Camera image of a doughnut intensity pattern. The star marks the center minimum. (B): Radial profile with the radius increasing from the center minimum. (C): The angles are defined anti-clockwise from the negative y-axis with respect to the central marker. The mean intensity of the bins is shown as the straight line and the RMSD can be calculated from the angular profile data.

and quarter-wave plates as specified by the manufacturer slightly differ from $\lambda/2$ and $\lambda/4$. The retardances at a wavelenght of 642 nm are 0.511λ and 0.269λ. Therefore, the half-wave plate was shifted as to obtain the maximum possible signal. This turned out to be at 314(1) deg which is consistent with the HWP specifications. The quarter-wave plate (QWP) situated right before the objective could only be set within an estimated error of about 5 deg. Therefore, the exact retardance of this wave plate did not play a role in acquiring circular polarization. By iteratively changing the angle of the QWP, a circular polarization of 80% was obtained.

Image analysis

The images as well as the theoretical models were processed using custom written MATLAB code. Angular and radial intensity profiles were made to analyse the aberrations observed in the doughnut profile. After determining the location of the center minimum by a parabolic fit, the intensity profile was split up in bins of equal angular separation. The angular profiles were used to determine the aberrations present in the system and to calculate the deviation from a rotational symmetric doughnut. The root-mean-squared deviation (RMSD) from the mean bin intensity was used as a measure for the mentioned deviation from symmetry. A non-ideal doughnut pattern has a corresponding varying angular intensity distribution and thus a high RMSD while an ideal dougnut is characterized by an equally distributed angular intensity. The radial profiles were obtained in a similar way, this time averaging the intensity over increasing radii from the center minimum.

Astigmatism-X (aX), Astigmatism-Y (aY), Coma-X (cX) and Coma-Y (cY) were in turn systematically varied as to minimize the RMSD of the mean angular intensity. This way, the SLM aberration parameters corresponding to the RMSD minima were used to optimize the rotational symmetry of the depletion beam.

Chapter 4

Results

In this section the results are shown and discussed. After aligning the setup and acquiring a circular polarization of 80%, the camera was used to capture images of doughut patterns with varying astigmatisms applied on the SLM. Thereby confirming the SLM's ability to shape foci and to get an insight in how doughnut shapes suffering from astigmatism look like. Assuming the setup was properly aligned, the phase mask on the SLM display was displaced as to align the beam's center minimum with the axis of propagation. Afterwards, beads were scanned to correct for astigmatism and coma. The theoretical model was compared to the measured radial profile of a scanned bead in order to confirm the reduced effective NA of the objective. The final results show doughnut profiles involving different polarizations.

4.1 Astigmatism Corrections

In 4.1b, the result of the calculated RMSDs with different values for astigmatism-X (aX) is shown. The minimum lies around aX= 0.1 and this value is set constant while varying aY (shown in figure 4.2b). Camera images of the extreme astigmatism values are also shown as to get an idea how astigmatism looks like on a doughnut shape. When astigmatism is present, the intensity is mainly situated on both sides of one axis through the center minimum. The SLM settings aX= 0.1 and aY= 0.0 will be used as a starting point when imaging and analysing beads.

(a) aX = −1.0, aY = 0.0

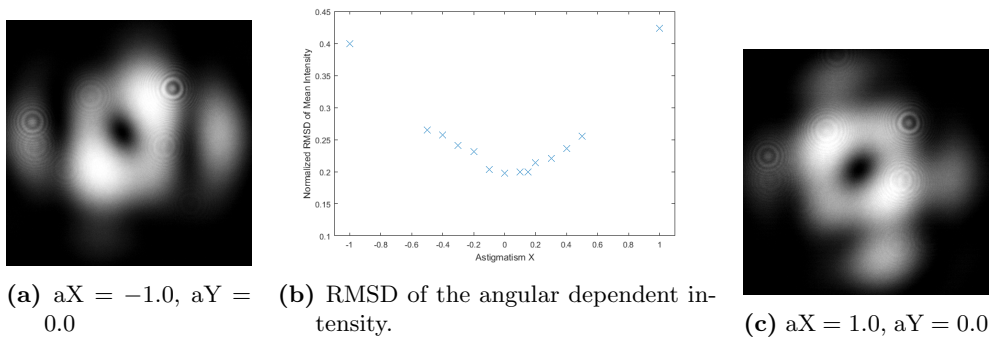(b) RMSD of the angular dependent intensity.

(c) aX = 1.0, aY = 0.0

Figure 4.1 – Camera captured doughnut patterns in which (a),(c) show clear oblique astigmatism (b) shows the RMSD as a function of the varying aX of which the minimum lies around aX = 0.1.
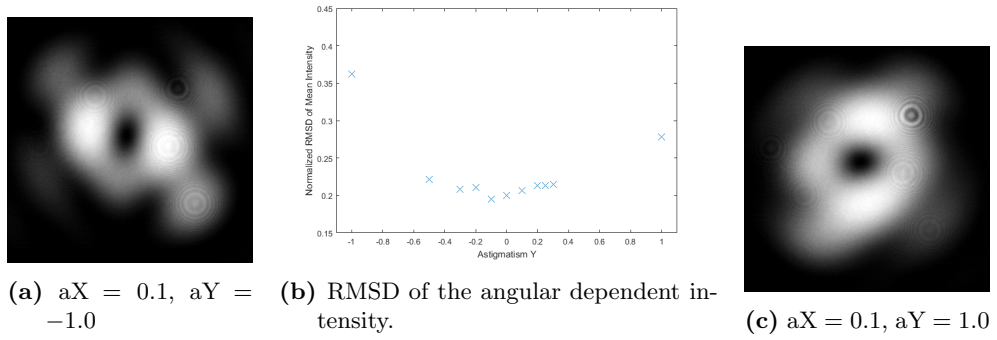
(a) aX = 0.1, aY = −1.0

(b) RMSD of the angular dependent intensity.

(c) aX = 0.1, aY = 1.0

Figure 4.2 – Camera captured doughnut patterns in which (a),(c) show clear vertical astigmatism (b) shows the RMSD as a function of the varying aY with aX = 0.1 of which the minimum lies around aY = 0.

(a) Misalign, before focus **(b)** Realign, before focus **(c)** Misalign, bead scan

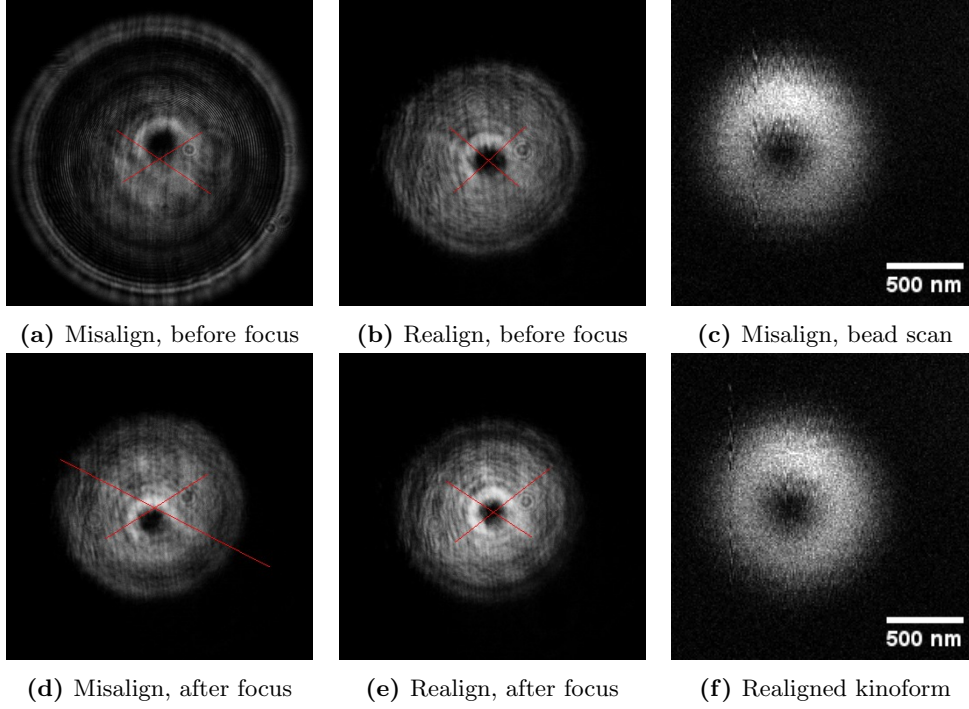**(d)** Misalign, after focus **(e)** Realign, after focus **(f)** Realigned kinoform

Figure 4.3 – Images of doughnut patterns with the beam focus before (a),(b) and after (d),(e) the camera image plane. Kinoform placement parameters when misaligned (a),(d) dx = 0.1, dy = 0.1 and realigned (b),(e) dx = 0.165, dy = 0.09. In (c) and (f) a scanned bead over an area of 2x2 µm is shown with and without realignment. The red crosses mark the lateral focus point.

4.2 Kinoform Alignment

After aligning the setup, it was possible to finetune the kinoform placement. A kinoform misalignment will cause the minimum of the doughnut to be out of center [REF]. When the beam hits the vortex phase mask on the SLM off-center, the center minimum will be off-axis. While propagating to the focus point of a lens, the center minimum will show a shift from its off-axis position to the focus point. After the focus, the center minimum will shift in opposite direction away from the axis. This effect could be easily observed by shifting in and out of focus at the PMT pinhole. Moreover, the off-center minimum was also observed at the iris right after the SLM. Therefore, other possible misalignments in the setup could not be the cause of this shift.

It was found that the kinoform suffered from a small misalignment. The alignment procedure was captured with the camera and is shown in figure 4.3.

Unfortunately, I did not find a way to properly quantify the actual distance corresponding to a kinoform replacement of dx= 0.01 and dy= 0.065 as applied on the SLM. I estimate the replacement to be in the order of millimeter or smaller.

Imaged beads before and after this alignment procedure are shown in figures 4.3c and 4.3f respectively. Before further aberration corrections are made, it can already be seen that the intensity distribution is less confined to one side of the doughnut.

4.3 Aberration Corrections by Scanning Beads

Beads were scanned with different values for aX and aY in order to minimize the RMSD. The results of these measurements are shown in figure 4.4. Graph 4.4a was obtained scanning a 2x2µm area using 200x200 pixels. Graph 4.4b and all following bead images were obtained scanning the same area size using 100x100 pixels. Although inconsistent,
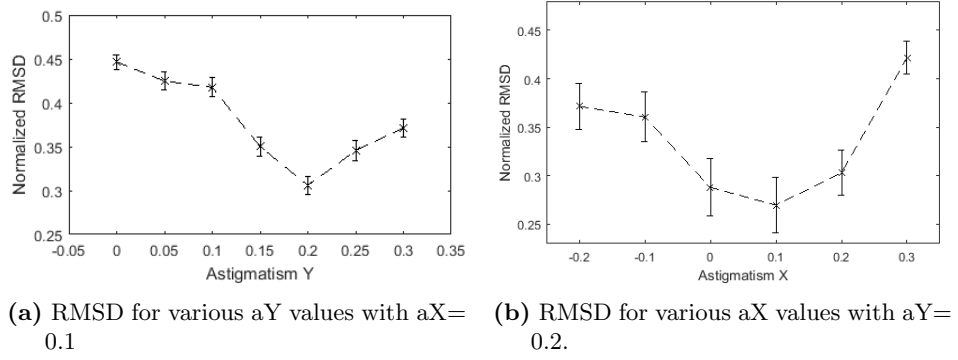
(a) RMSD for various aY values with aX= 0.1

(b) RMSD for various aX values with aY= 0.2.

Figure 4.4 – Minimization of the RMSDs leading to aX = 0.1 and aY= 0.2.
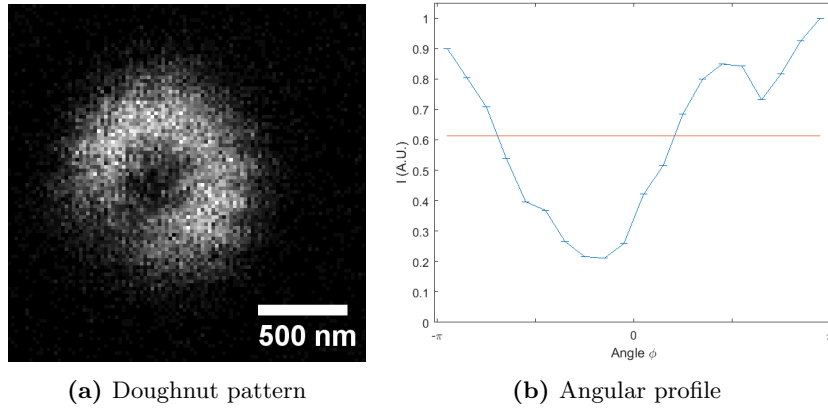

(a) Doughnut pattern

(b) Angular profile

Figure 4.5 – (A) doughnut pattern with aX= 0.1 and aY= 0.2 and (b) it's angular profile.

the measurments took a lot of time and therefore I decided to reduce the number of pixels per scan. This also shows up in the larger errorbars in the graphs.

The analysis of the scanned beads results in an slightly different vertical astigmatism than obtained with the camera. This is probably due to sample induced aberrations.
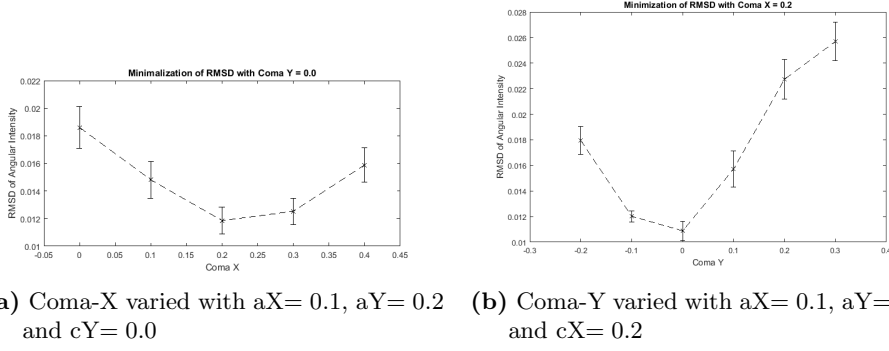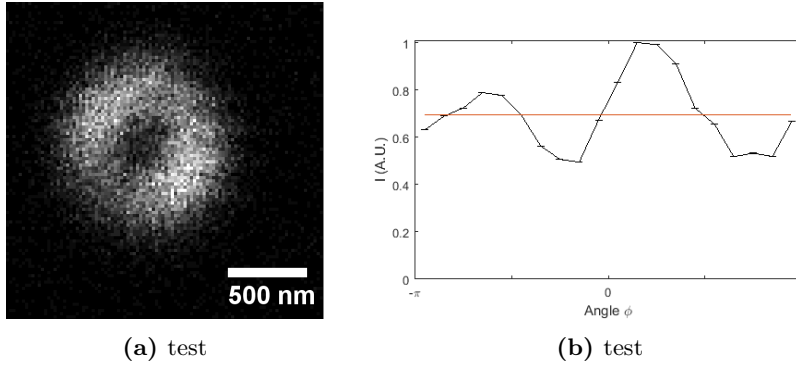
(a) Coma-X varied with aX= 0.1, aY= 0.2 and cY= 0.0

(b) Coma-Y varied with aX= 0.1, aY= 0.2 and cX= 0.2

Figure 4.6 – Coma

(a) test

(b) test

Figure 4.7 – Imaged bead (a) and angular profile (b) with aX= 0.1, aY= 0.2 and cX= 0.0

4.3.1 Coma Corrections

After attempting to obtain a symmetric doughnut by making astigmatism corrections on the SLM, there was still an obvious asymmetry in the intensity distribution. Now, Zernike Polynomials of both astigmatisms show a two-fold symmetry in perpendicular axis as was also observed in 4.2. However, the asymmetry still present was mainly a one-sided intensity peak i.e. a single axis symmetry. Coma, which shows this single axis symmetry as well, was used to correct for the asymmetry unable to resolve with astigmatism corrections.

The result of the RMSD minimization after coma corrections is shown in figure 4.6. The new SLM settings for which aberrations are minimized are now aX= 0.1, aY= 0.2, cX= 0.2 and cY= 0.0.

Though, if we look at the angular profile it is clear that some astigmatism is still disturbing the doughnut shape. It looks like as if I overcorrecting the doughnut shape by applying too much astigmatism. Looking at figure 4.7, the bead and angular profile show some oblique astigmatism as earlier encountered in the camera pictures.

Also, from table 2.1 in the theory section, the angular term in the Zernike polynomial corresponding to oblique astigmatism $Z_2^{-2} \propto \sin 2\phi$ is present in the angular profile. Unfortunately, I did not quantify the relation between the SLM parameters for aberration corrections and the observed angular intensity distributions. Therefore, a final correction should be an adjustment of the Astigmatism-X parameter.

The imaged bead at aX= 0.0 is shown in between an imaged bead with a slightly lower and higher aX value which show opposite oblique astigmatism. Therefore, the SLM corrections are now set to aX= 0.0, aY= 0.2, cX== 0.2 and cY= 0.0.

Further minimization could be done by analyzing the angular profile to see if there are more periodic patterns present. Since astigmatism and coma show up as a double and single periodicity in the intensity distribution I could also have tried to retrieve the SLM correction settings from fitting the angular terms of the corresponding Zernike
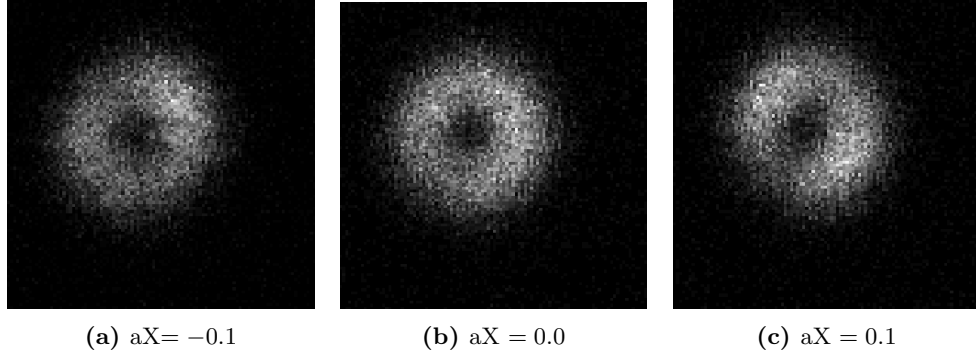
(a) aX= −0.1   (b) aX = 0.0   (c) aX = 0.1

Figure 4.8 – Imaged beads with SLM settings aY= 0.2, cX== 0.2, cY= 0.0 and varying aX.
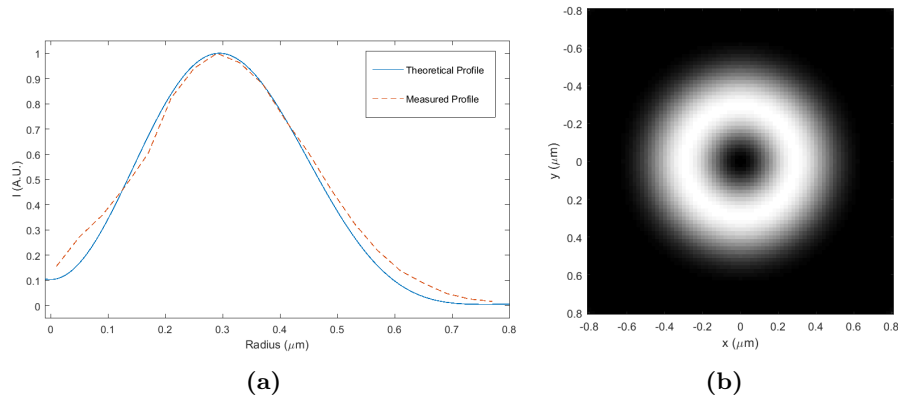

(a)   (b)

Figure 4.9 – The effective NA is assumed to be 0.86. (A) a plot of the theoretical model and the experimental data and (b) an ideal depletion beam.

Polynomials. As already mentioned, in future experiments, a quantified relation between the SLM settings and the angular intensity distribution could be found in order retrieve the correct SLM settings within only a few scans of beads.

4.3.2 Effective NA and Model Limitations

The theoretical model is used to see how the angular profile behaves in case of an incorrect center minimum determination. In the experimental data, the pixelized nature of the scanned bead images, small vibrations and a non-zero center minimum all contribute to an estimated uncertainty of ± 1 pixel in the determination of the center minima.

To compare the experimental data with the theoretical model, the radial profiles are plotted together in figure 4.9. Since the scanned beads have a finite size of 200 µm, the convolution of the theoretical model with the bead is taken into account. Moreover, the objective was underfilled by a factor of 0.72(2). Following the reasoning of de Boer [2015], I assume that the effective NA scales linearly with the beam radius. The effective NA used in the model is therefore 0.86(2).

The radial profiles of the theoretical and experimental data show a difference of the peak radii of less than 3%. This differs from earlier done measurements by B. Brouwer using this same setup and sample. He estimated the effective NA to be around 0.97(3). A possible explanation for this difference is that in both cases only a single bead was used. Multiple beads have to be scanned in order to get an idea of the variation of their radii.

Angular profiles were made for an ideal depletion beam with a NA of 0.86 together with an angular profile of the corrected doughnut pattern of figure 4.8c. The minimum bin value for the corrected doughnut lies around 0.7 times the maximum value. However,
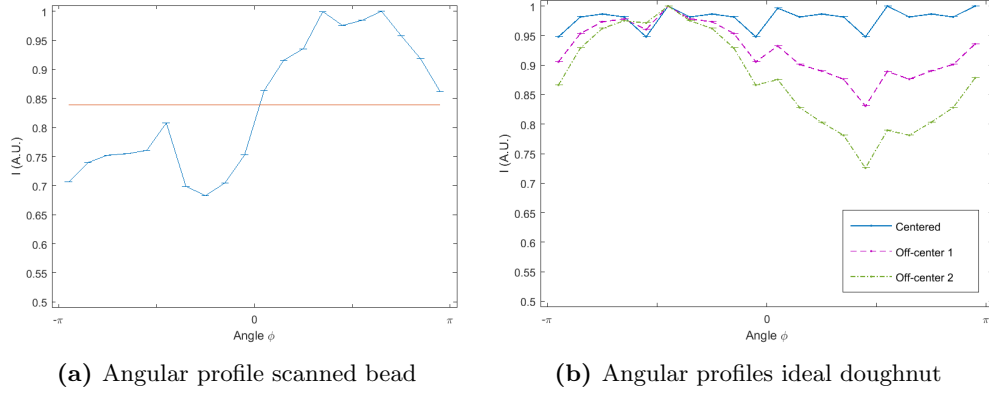
(a) Angular profile scanned bead   **(b)** Angular profiles ideal doughnut

Figure 4.10 – Angular profile (a) with aX= 0.1, aY= 0.2 and cX= 0.0 and angular profiles of an ideal depletion beam (b) with the center minimum shifted 1 pixel (20 nm) and 2 pixels (40 nm).
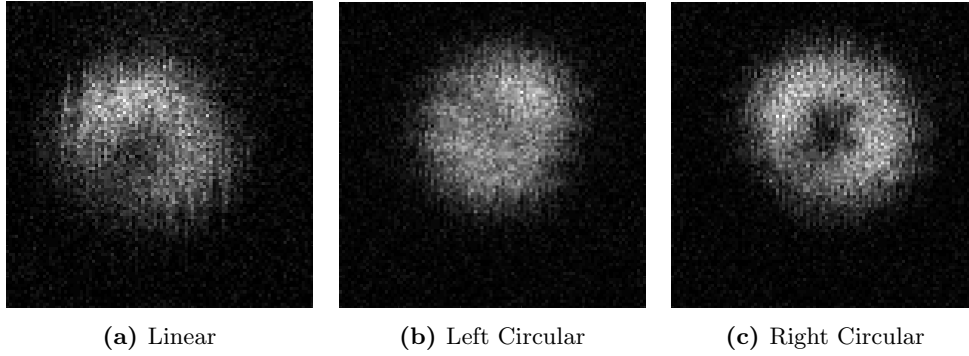

(a) Linear   **(b)** Left Circular   **(c)** Right Circular

Figure 4.11 – Imaged beads with left- and right-handed circular and linear polarizations. SLM settings aX= 0.15, aY= 0.2, cX= 0.0 and CY= 0.0

the ideal doughnut profiles in figure 4.10b show a minimum bin value around 0.85 and 0.7 times the maximum intensity. Therefore, if the intensity variation of the scanned beads lies within 15%, the method of aberration analysis I used is insufficient. This also suggests that the final doughnut pattern (figure 4.8c and 4.10b) still suffers from some small aberrations or misalignments since the intensity variation is greater than 15% of the maximum.

Polarization

Since simulations Hao, Kuang, Wang, and Liu [2010] and previously done experiments Yang et al. [2016] show that circular polarization will give the best doughnut shape, I tried to obtain circular polarization and observe the shape of differently polarized beams.

The linear polarized doughnut is stretched out with a high intensity region in the upper left area of the doughnut. This is probably due to the wrong aberration corrections as these experiments were done before the coma corrections were obtained. The left-handed circular polarized doughnut is distorted in a way that it would be useless as a depletion beam. There is no center minimum present. The right-handed circularly polarized doughnut does show a center minimum and a ring shaped intensity surrounding it. Therefore, I used circularly polarized light in all other measurements.

4.4 Conclusion and Discussion

First of all, it can be concluded that the SLM could be used to shape foci in an almost arbitrary way by modulating the phase of light. Phase masks for a doughnut shaped

depletion beam as well as aberration corrections could all easily be generated by the SLM. It was found that the depletion beam deviated form it's rotational symmetry due to a combination of aberrations and misalignments in the setup. After mechanical alignment, the kinoform's positioning appeared to cause an increased intensity on one side of the ring. Realigning the kinoform reduced this one sided intensity increase. Via the analysis of the angular profiles of scanned beads I found that small amounts of astigmatism and coma were present in the setup and the SLM could be used to correct for these aberrations. Also, the angular terms of the Zernike Polynomials for coma and astigmatism were used to distinguish the two from eachother. In turn, the SLM was used to systematically correct for these aberrations. In the end, the depletion beam still showed some asymmetry which I was unable to resolve since time runned out. However, due to the uncertainty in the center minimum determination, the method used to analyse the depletion beam may be insufficient when the difference between the angular bins of maximum and minimum intensity is less than 15%. Several factors may affect the rotational symmetry optimization of the depletion beam: The way in which angular profiles were calculated, the pixel nature of the images and small misalingments limited the aberration analysis. In future experiments, a quantified relation between the SLM parameters for the aberration phase masks and the angular intensity distribution could be found in order to correct for the aberrations present within only a few scans of beads.

Bibliography

History of the microscope, http://www.history-of-the-microscope.org/anton-van-leeuwenhoek-microscope-history.php, accessed: 2016-06-15.

R. R. Dijkstra, Master's thesis, University of Twente (2012).

E. Abbe, in *Proceedings of the Bristol Naturalists' Society* (1874), vol. 1, pp. 200–261.

S. W. Hell and J. Wichmann, Optics letters **19**, 780 (1994).

M. Born and E. Wolf, *Principles of optics: electromagnetic theory of propagation, interference and diffraction of light* (CUP Archive, 2000).

A. de Boer, Master's thesis, University of Utrecht (2015).

B. Neupane, F. Chen, W. Sun, D. T. Chiu, and G. Wang, Review of Scientific Instruments **84**, 043701 (2013).

J. Leach, M. Dennis, J. Courtial, and M. Padgett, New Journal of Physics **7**, 55 (2005).

J. C. Wyant and K. Creath, Applied optics and optical engineering **11**, 2 (1992).

Zernike aberrations, http://www.telescope-optics.net/zernike_aberrations.htm, accessed: 2016-06-15.

Zernike polynomials, https://en.wikipedia.org/wiki/Zernike_polynomials, accessed: 2016-06-15.

H. Yang, Y. Zhang, Y. Xiao, F. Gao, J. Chang, T. Wei, and S. Jiang, Optik-International Journal for Light and Electron Optics (2016).

X. Hao, C. Kuang, T. Wang, and X. Liu, Journal of Optics **12**, 115707 (2010).

Acknowledgements